7

HIGH-RESOLUTION SPECTROSCOPY

1. Introduction

In 1896, P. Zeeman observed that when a sodium source was placed in a strong magnetic field, the yellow D lines were split into several components. Faraday had performed the same experiment some thirty years earlier but had failed to observe an effect because of the low resolution of his spectrograph. We also know from Chapter 2 (4.3) that even in the absence of a magnetic field the atomic spectral lines have a fine structure which was easily observed with the small grating spectrometer; with a high-resolution instrument, however, it becomes possible to observe that each of these fine structure lines may again be resolved into closely spaced components, which form the so-called "hyperfine structure" (hfs) of atomic lines.[†]

The splitting of a spectral line obviously is a consequence of a splitting of the initial state, or of the final state, or of both states between which

[†] To set the reader at ease, no further splitting beyond the hyperfine structure has been observed, nor can it be expected for free atoms; in the hyperfine structure we include both the splitting due to *nuclear spin* and that due to *isotope shift*.

the transition takes place. The energy-level splittings produced by the application of an external magnetic field $\mathbf{H}$ (Zeeman effect) are of the order of

$$\Delta E = \mathbf{\mu} \cdot \mathbf{H} = \frac{e}{2m_e c} \mathbf{L} \cdot \mathbf{H} \sim \frac{e\hbar}{2m_e c} H \tag{1.1}$$

where $\mathbf{\mu}$ is the magnetic moment of the state (see Section 2 of this chapter). The constant $\mu_0 = e\hbar/2mc = 0.579 \times 10^{-14}$ MeV/gauss is called the Bohr magneton, so that in units of wave numbers the displacement for *one* Bohr magneton is

$$\Delta \bar{\nu} = \frac{\Delta \nu}{c} = \frac{\Delta E}{hc} = \frac{e}{4\pi m_e c^2} H = 4.669 \times 10^{-5} \times H \text{ cm}^{-1} \tag{1.2}$$

with H in gauss.

The hyperfine structure splitting is due to the interaction of the magnetic-dipole, electric-quadrupole, etc., moment of the nucleus, with the electromagnetic field produced by the electrons at the nucleus. The interaction energy for the magnetic dipole term is of the order of

$$\Delta E = \mathbf{\mu}_N \cdot \langle \mathbf{H}_J(0) \rangle \sim \mu_N \mu_0 \left\langle \frac{1}{r^3} \right\rangle = \frac{\mu_0^2}{1837} \left\langle \frac{1}{r^3} \right\rangle \tag{1.3}$$

where μ_N is the nuclear magneton

$$\mu_N = \frac{e\hbar}{2mc} = \frac{\mu_0}{1837}$$

and $\langle \mathbf{H}_J(0) \rangle$ is the expectation value for the magnetic field of the electrons at the origin; it is equal to $\mu_0 \langle 1/r^3 \rangle$ (except for configurations with $l = 0$). Instead of evaluating $\langle 1/r^3 \rangle$, we recall that the fine structure splitting is due to an $\mathbf{L} \cdot \mathbf{S}$ coupling of the electrons, and therefore is of the order of $\mu_0^2 \langle 1/r^3 \rangle$, so that we expect

$$\Delta E(hfs) \sim \frac{\Delta E(\text{fs})}{1837} \tag{1.4}$$

Let us substitute reasonable numbers in Eqs. 1.2 and 1.4; for example, $H \approx 10$ kilogauss yields

$$\Delta \bar{\nu}(\text{Zeeman}) \sim 0.460 \text{ cm}^{-1}$$

and[†] $\Delta \bar{\nu}$ (fine structure) ~ 100 cm^{-1} yields

$$\Delta \bar{\nu}(\text{hfs}) = 0.050 \text{ cm}^{-1}$$

[†] See for example Chapter 2, p. 47.

Thus the splitting of the lines is very small and can be observed only with a high-resolution instrument. Assuming $\lambda \approx 5000$ Å and $\Delta\bar{\nu} \sim 0.050$ cm^{-1}, we find that the required resolving power is

$$\frac{\lambda}{\Delta\lambda} = \frac{\bar{\nu}}{\Delta\bar{\nu}} = 4 \times 10^5$$

Such resolution may be achieved in two ways:

(a) With a large grating used in a high order; the resolving power of a grating is given by

$$\frac{\lambda}{\Delta\lambda} = Nn$$

where n, the diffraction order, can be as large as 20, and for a 10-in. grating with 7000 rulings to the inch, the number of rulings is $N = 7 \times 10^4$, so that

$$\frac{\lambda}{\Delta\lambda} \sim 10^6$$

Such gratings, are, however, very difficult to construct, but can now be obtained commercially.

(b) With a "multiple beam" interferometer; the most common one today and easiest to use being the Fabry-Perot. It consists of two reflecting glass plates of high quality which are kept parallel and at a distance t. The interference pattern appears as a series of concentric rings, and the resolution, the so-called "instrument width" is

$$\delta\bar{\nu} = \frac{1}{2t} \frac{1 - R}{\pi\sqrt{R}} \tag{1.5a}$$

where R is the reflectivity of the plates. It is more helpful to use the expression

$$\Delta\bar{\nu} = \Delta n \frac{1}{2t} \tag{1.5b}$$

where Δn is the fraction of an order by which the ring has been shifted. It is easy to distinguish $\Delta n \sim 1/10$, and t can be as large† as 2 cm, so that

$$\Delta\bar{\nu} = 25 \times 10^{-3} \text{ cm}^{-1}$$

which for $\lambda = 4000$ Å corresponds to $\lambda/\Delta\lambda \approx 10^6$. An additional require-

† In special cases connected with the observation of lasers, spacings as large as 1m have been used.

ment for the observation of such small structure of spectral lines is that the lines themselves be narrower than the spacing between the components of the structure. For that purpose special light sources have been constructed which emit lines that are as narrow as possible.

In this chapter we first present an elementary discussion of the theory of the Zeeman effect and of the theory of hyperfine structure. A brief section is devoted to light sources, and next the Fabry-Perot interferometer is described. In Section 6, experimental data on the Zeeman effect of the 5461-Å green line of Hg^{198}, obtained with a Fabry-Perot, are treated in detail. Next, the medium-resolution grating spectrograph used in this laboratory is described and data on the Zeeman effect obtained with it, are presented; finally data on the hyperfine structure of mercury obtained with a grating of high quality are also presented.

REFERENCES

By necessity the discussion of certain topics in this chapter is very brief. However the bibliography on atomic spectroscopy is excellent and extensive. The following texts and monographs should be very useful to the student.

E. U. Condon and G. H. Shortley, *The Theory of Atomic Spectra*, Oxford Univ. Press. This is one of the most complete theoretical treatments on atomic spectroscopy, but at an advanced level.

H. E. White, *Introduction to Atomic Spectra*, McGraw-Hill. This book contains extensive data on atomic spectra and the treatment of the theory is based on the semiclassical approach of the vector model.

H. Kuhn, *Atomic Spectra*, Longman's, London, 1962. A recent good book on a slightly more advanced level than White's book, referred to above.

S. Tolansky, *High Resolution Spectroscopy*, Methuen, London. A very comprehensive and clear treatise on the instruments and techniques of high-resolution spectroscopy.

H. Kopferrnan, *Nuclear Moments*, Academic Press. This book contains a very complete discussion of atomic hyperfine structure, of analysis methods, and of the conclusions that are obtained from it.

2. The Zeeman Effect

2.1 THE NORMAL ZEEMAN EFFECT

As already discussed in Chapter 2, Section 4, the solution of the Schrödinger equation† yields "stationary states" labeled by three integer indices, n, l, and m, where $l < n$ and $m = -l, -l + 1, \cdots, l - 1, l$. For the screened Coulomb potential, the energy of these states depends on n and l but not on m; we therefore say that the $(2l + 1)$ states with the same

† See, for example, E. Fermi, *Notes on Quantum Mechanics*, Univ. of Chicago Press, or any other text on quantum mechanics.

n and l index are "degenerate" in the m quantum number. Classically we can attribute this degeneracy to the fact that the plane of the "orbit" of the electron may be oriented in any direction without affecting the energy of the state, since the potential is spherically symmetric.

If now a magnetic field H is switched on in the region of the atom, we should expect that the electrons (and the nucleus†) will interact with it. We need only consider the electrons outside closed shells, and let us assume there is one such electron; indeed the interaction of the magnetic field with this electron yields for each state an additional energy ΔE, given by

$$\Delta E = m\mu_0 H \tag{2.1}$$

Thus, the total energy of a state depends now on n, l, and m, and the degeneracy has been removed.
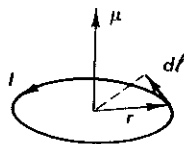

FIG. 7.1   Magnetic moment due to a current circulating in a closed loop.

To see how this additional energy arises we consider again the classical analogy. Then the orbiting electron is equivalent to a current density‡

$$\mathbf{J}(\mathbf{x}) = -e\mathbf{v}\,\delta(\mathbf{x} - \mathbf{r})$$

where $\mathbf{r}$ is the equation of the orbit and $\mathbf{x}$ gives the position of the electron; the negative sign obviously arises from the negative charge of the electron. Such a current density gives rise to a magnetic dipole moment

$$\mathbf{\mu} = \frac{1}{2c}\int \mathbf{x} \times \mathbf{J}(\mathbf{x})\, d^3x = -\frac{1}{2c}\,e(\mathbf{r} \times \mathbf{v})$$

---

† For our present discussion this interaction of the nucleus with the external field is so small that we will neglect it.

‡ For a circular orbit, the electron is equivalent to a current $I = \Delta Q/\Delta T = e/T = e\omega/2\pi$ where ω is the angular frequency $\omega = v/a$; a is the radius of the orbit. But a plane closed loop of current gives rise to a magnetic moment $\mu = (I/c)A$ where A is the area enclosed by the loop; in our case $A = \pi a^2$, hence

$$\mu = \frac{ev}{2\pi ac}\,\pi a^2 = \frac{eva}{2c}$$

The angular momentum for the circular orbit is $L = m_e v a$, hence

$$\mu = \frac{e}{2m_e c}\,L$$

as in Eq. 2.2.

But the angular momentum of the orbit is given by

$$\mathbf{L} = \mathbf{r} \times \mathbf{p} = m_e(\mathbf{r} \times \mathbf{v})$$

so that

$$\mathbf{\mu} = -\frac{e}{2m_e c}\,\mathbf{L} = -\frac{e\hbar}{2m_e c}\,l\mathbf{u}_L \tag{2.2}$$

where we expressed the angular momentum of the electron in terms of its quantized value (according to Bohr) $L = lh/2\pi$ and $\mathbf{u}_L$ is a unit vector along the direction of $\mathbf{L}$. Now, the energy of a magnetic dipole in a homogeneous field is

$$E = -\mathbf{\mu}\cdot\mathbf{H} = \frac{e}{2m_e c}\,\mathbf{L}\cdot\mathbf{H} \tag{2.3}$$

but the angle between $\mathbf{L}$ and the external field $\mathbf{H}$ cannot take all possible values.† We know that it is quantized, so that the projection of $\mathbf{L}$ on the z axis (which we can take to coincide with the direction of $\mathbf{H}$ since no other preferred direction exists) can only take the values $m = -l, -l + 1, \cdots, l - 1, l$. Thus, the energy of a particular state n, l, m in the presence of a magnetic field will be given by‡

$$E_{n,l,m} = -E_{n,l} + mH\mu_0 \tag{2.4}$$

where§

$$\mu_0 = \frac{e\hbar}{2m_e c}$$

In Fig. 7.2 is shown the energy-level diagram for the five states with given n and $l = 2$, before and after the application of a magnetic field H. We
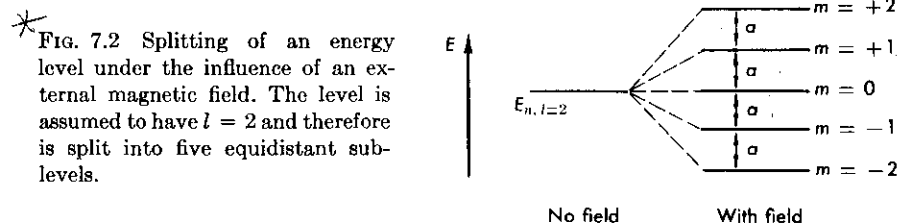

FIG. 7.2   Splitting of an energy level under the influence of an external magnetic field. The level is assumed to have $l = 2$ and therefore is split into five equidistant sublevels.

---

† This was first clearly shown in the Stern-Gerlach experiment.

‡ The energy in the field is $+(e\hbar/2m_e c)m$ because the electron charge is taken as negative.

§ In the MKS system $\mu_0 = (e\hbar/2m_e)$; m_e in this expression is obviously the mass of the electron, not to be confused with the magnetic quantum number m.

(a)   (b)   (c)
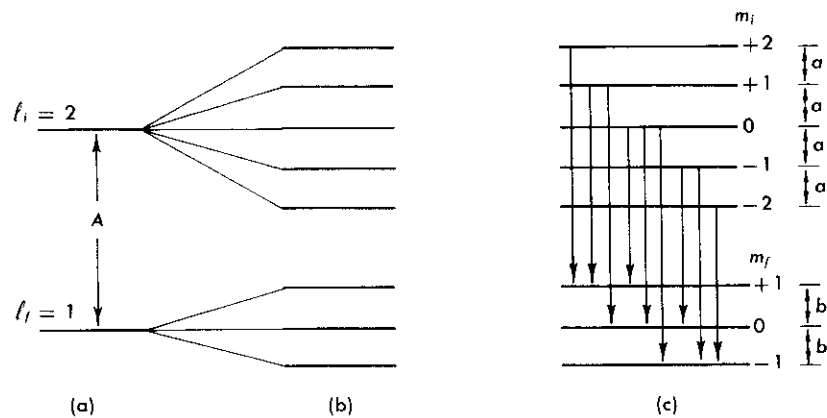
Fig. 7.3 Splitting of a spectral line under the influence of an external magnetic field. (a) The initial level ($l = 2$) and the final level ($l = 1$) with no magnetic field are shown. A transition between these levels gives rise to the spectra line. (b) The two levels after the magnetic field has been applied. (c) The nine allowed transitions between the eight sublevels of the initial and final state.

note that all the levels are equidistantly spaced, the energy difference between them being

$$\Delta E = \mu_0 H$$

Let us next consider the transition between a state with n_i, l_i, m_i and one with n_f, l_f, m_f. As an example we choose $l_i = 2$ and $l_f = 1$, and the energy-level diagram is shown in Fig. 7.3; without a magnetic field in Fig. 7.3a, and when the magnetic field is present in Fig. 7.3b.

However, we know that for an electric dipole transition to take place between two levels, certain selection rules must be fulfilled: in particular,

$$\Delta l = \pm 1 \tag{2.5}$$

Thus, when the field is turned on, we cannot expect transitions between the m sublevels with the same l, since they do not satisfy Eq. 2.5. Further, also the transitions between the sublevels with $l_i = 2$ to the sublevels with $l_f = 1$ which do satisfy Eq. 2.5 are now governed by the *additional* selection rule†

$$\Delta m = 0, \qquad \pm 1 \tag{2.6}$$

and thus only the transitions shown in Fig. 7.3c are allowed.

Let the energy splitting in the initial level be a, and in the final level be b, and let A be the energy difference between the two levels when no

---

† The selection rules of atomic spectroscopy are a consequence of the addition of angular momenta. In this specific case the selection rules indicate that we consider only *electric dipole* radiation.

TABLE 7.1

ALLOWED TRANSITIONS FROM $l_i = 2$ TO $l_f = 1$ AND THE CORRESPONDING ENERGIES

m of final state	m of initial state				
	+2	+1	0	−1	−2
+1	$A + 2a - b$	$A + a - b$	$A - b$	×	×
0	×	$A + a$	A	$A - a$	×
−1	×	×	$A + b$	$A - a + b$	$A - 2a + b$

Note: An X indicates that this particular transition may not take place.

magnetic field is applied. Then the energy released in a transition $i \rightarrow f$ is given by

$$E_i - E_f = A_{if} + m_i a - m_f b \tag{2.7}$$

These energy differences for the nine possible transitions shown in Fig. 7.3c, are given in matrix form in Table 7.1; an × indicates that the transition is forbidden and will not take place.

At this point the reader must be concerned about the use of a and b; according to our previous argument (Eq. 2.4), as long as all levels are subject to the same magnetic field H, their splitting must also be the same, and

$$a = b = \mu_0 H$$

Thus, we see from Eq. 2.7 (or Table 7.1) that only *three* energy differences are possible

$$E_i - E_f = A + a(m_f - m_i) = A + a\Delta m$$

where Δm is limited by the selection rule, Eq. 2.6, to the *three* values +1, 0, −1. Consequently, in the presence of a magnetic field H, the single spectral line of frequency $\nu = A/h$ is split into three components with frequencies

$$\nu_- = (A - \mu_0 H)/h, \qquad \nu_0 = A/h, \qquad \text{and} \qquad \nu_+ = (A + \mu_0 H)/h$$

irrespective of the values of l_i and l_f. Furthermore, these spectral lines are polarized, as shown in Fig. 7.4. When the Zeeman effect is viewed in a direction *normal* to the axis of the magnetic field, the central component is polarized parallel to the axis whereas the two outer ones normal to the axis of the field. When the Zeeman effect is observed *along* the axis of the the field (by making a hole in the pole face, or using a mirror), only the two outer components appear, circularly polarized. The lines from

$\Delta m = +1$ transitions appear with right-hand circular polarization; from $\Delta m = -1$ transitions, with left-hand circular polarization. The central line does not appear, since the electromagnetic field must always have the field vectors ($\mathbf{E}$ and $\mathbf{B}$) normal to the direction of propagation.
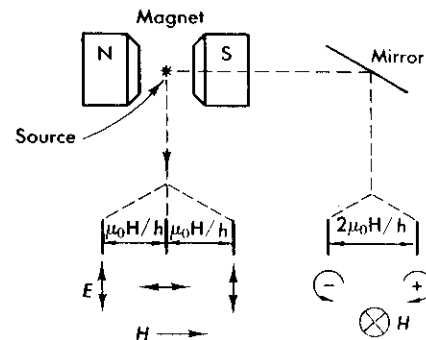
FIG. 7.4 The polarization and separation of the components of a normal Zeeman multiplet when viewed in a direction normal to, and in a direction parallel to, the magnetic field.

The splitting of a spectral line into a triplet under the influence of a magnetic field is called the *"normal"* Zeeman effect, and is occasionally observed experimentally, as, for example, in the 5790 Å line of mercury arising in a transition† from $^1D_2$ to $^1P_1$. But in most cases the lines are split into more components, and even where a triplet appears it does not always show the spacing predicted by Eq. 2.4. This is due to the intrinsic magnetic moment of the electron (associated with its spin) and will be discussed in the following sections.

2.2 THE INFLUENCE OF THE MAGNETIC MOMENT OF THE ELECTRON

In Chapter 2 it was discussed how the intrinsic angular momentum (spin) of the electron $\mathbf{S}$ couples with the orbital angular momentum of the electron $\mathbf{L}$ to give a resultant $\mathbf{J}$; this coupling gave rise to the "fine structure" of the spectra‡. The projections of $\mathbf{J}$ on the z axis are given by m_J and we could expect (on the basis of our previous discussion) that the *total* magnetic moment of the electron will be given by

$$\mathbf{\mu} = \frac{\mu_0}{\hbar} \mathbf{J} \tag{2.8}$$

† Note that both initial and final state have $S = 0$.

‡ We will use the following notation: $\mathbf{L}$, $\mathbf{S}$, $\mathbf{J}$ represent the angular momentum vectors which have magnitude $\hbar\sqrt{l(l+1)}$, $\hbar\sqrt{s(s+1)}$, $\hbar\sqrt{j(j+1)}$.

The symbols l, j, etc. (s is always $s = \frac{1}{2}$) are the *quantum numbers* which label a one-electron state and appear in the above square root expressions.

The symbols L, S, J, etc., are the *quantum numbers* which label a state with more than one electron and are then used instead of l, s, j.

Consequently, the energy-level splitting in a magnetic field H would be in analogy to Eq. 2.4,

$$\Delta E = -m_J \mu_0 H \tag{2.9}$$

These conclusions, however, are not correct because the *intrinsic* magnetic moment of the electron is related to the *intrinsic* angular momentum of the electron (the spin) through

$$\mathbf{\mu}_e = 2\frac{e}{2m_e c}\mathbf{S} = 2\frac{e\hbar}{2m_e c}s\mathbf{u}_s \tag{2.10}$$

and *not* according to Eq. 2.2.† Consequently, the *total* magnetic moment of the electron is given by the operator

$$\mathbf{\mu} = (\mu_0/\hbar)[\mathbf{L} + 2\mathbf{S}] \tag{2.11}$$

We can think of it as a vector oriented along $\mathbf{J}$ but of magnitude

$$\mu = \mu_0 gJ \tag{2.12}$$

The numerical factor g is called the Landé g factor and a correct quantum-mechanical calculation gives‡

$$g = 1 + \frac{j(j+1) + s(s+1) - l(l+1)}{2j(j+1)} \tag{2.13}$$

---

† The result of Eq. 2.10 is obtained in a natural way from the solution of the Dirac equation; also from the classical relativistic calculation of the "Thomas precession."

‡ This result can also be obtained from the vector model for the atomic electron. In Fig. 6.5 the three vectors $\mathbf{J}$, $\mathbf{L}$, and $\mathbf{S}$ are shown, and $\mathbf{L}$ and $\mathbf{S}$ couple into the resultant $\mathbf{J}$, so that

$$\mathbf{J} = \mathbf{L} + \mathbf{S}$$

By taking the squares of the vectors, we obtain the following values for the cosines

$$\cos(\mathbf{L}, \mathbf{J}) = \frac{j^2 + l^2 - s^2}{2lj} \qquad \cos(\mathbf{S}, \mathbf{J}) = \frac{j^2 + s^2 - l^2}{2sj}$$

From Eq. 2.11 we see that

$$\mu/\mu_0 = l\cos(\mathbf{L}, \mathbf{J}) + 2s\cos(\mathbf{S}, \mathbf{J})$$

Thus

$$g = \frac{\mu}{\mu_0 j} = \frac{j^2 + l^2 - s^2}{2j^2} + \frac{2j^2 + 2s^2 - 2l^2}{2j^2} = 1 + \frac{j^2 + s^2 - l^2}{2j^2}$$
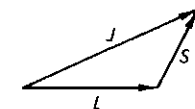
FIG. 7.5 Addition of the orbital angular momentum $\mathbf{L}$, and of the spin angular momentum $\mathbf{S}$ into the total angular momentum $\mathbf{J}$, according to the "vector model."

Finally we must replace j^2, s^2, and l^2 by their quantum mechanical expectation values $j(j+1)$, etc., and we obtain Eq. 2.13.

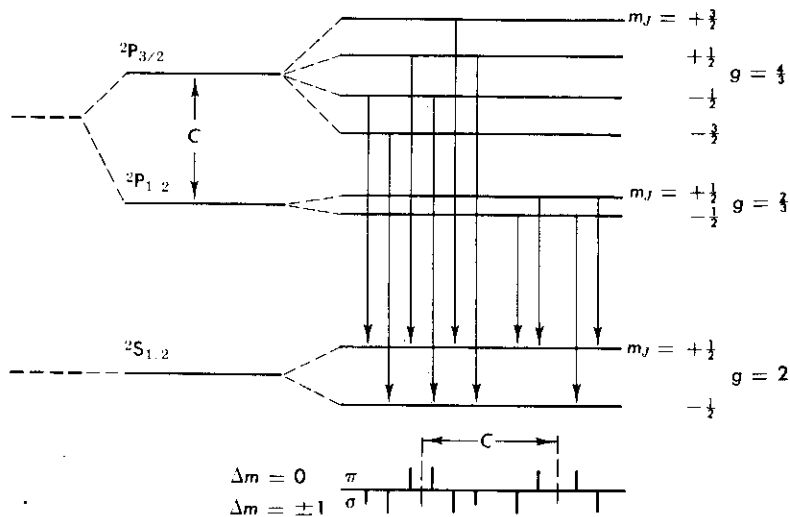$\Delta m = 0 \quad \pi$

$\Delta m = \pm 1 \quad \sigma$

FIG. 7.6 Energy levels of a single valence electron atom showing a P state and an S state. Due to the fine structure, the P state is split into a doublet with $j = \frac{3}{2}$ and $j = \frac{1}{2}$. Further, under the influence of an external magnetic field each of the three levels is split into sublevels as shown in the figure where account has been taken of the magnetic moment of the electron. The magnetic quantum number m_j for each sublevel is also shown as is the g factor for each level. The arrows indicate the allowed transitions between the initial and final states, and the structure of the line is shown in the lower part of the figure.

The interesting consequence of Eqs. 2.12 and 2.13 is that now the splitting of a level due to an external field H is

$$\Delta E = (g\mu_0 H)m_j \tag{2.14}$$

and in contrast to Eq. 2.4 is *not* the same for all levels; it depends on the j and l of the level ($s = \frac{1}{2}$ always when one electron is considered). The sublevels are still equidistantly spaced but by an amount

$$\Delta E = g\mu_0 H$$

Let us then consider again the transitions between sublevels belonging to two states with different l (in order to satisfy Eq. 2.5). Since, however, we are taking into account the electron spin, l is not a good quantum number, and instead the j values of the initial and final level must be specified. If we choose for this example $l_i = 1$ and $l_f = 0$, we have the choice of $j_i = \frac{3}{2}$ or $j_i = \frac{1}{2}$, whereas $j_f = \frac{1}{2}$. Transitions may occur only if they satisfy, in addition to Eq. 2.5, *also* the selection rules for j

$$\Delta j = 0, \pm 1 \quad \text{not} \quad j = 0 \to j = 0 \tag{2.5a}$$

Furthermore the selection rules for m_j must also be satisfied; they are the same as given by Eq. 2.6

$$\Delta m_j = 0, \pm 1 \tag{2.6a}$$

In Fig. 7.6 the energy-level diagram is given without and with a magnetic field for the doublet initial state with $l = 1$, and the singlet final state, $l = 0$. Six possible transitions between the initial states with $j = \frac{3}{2}$ to the final state with $j = \frac{1}{2}$ are shown (as well as the four possible transitions from $j = \frac{1}{2}$ to $j = \frac{1}{2}$). By using Eq. 2.13 we obtain the following g factors

$$l = 1 \qquad j = \tfrac{3}{2} \qquad s = \tfrac{1}{2} \qquad g = \tfrac{4}{3}$$

$$l = 1 \qquad j = \tfrac{1}{2} \qquad s = \tfrac{1}{2} \qquad g = \tfrac{2}{3}$$

$$l = 0 \qquad j = \tfrac{1}{2} \qquad s = \tfrac{1}{2} \qquad g = 2$$

The sublevels in Fig. 7.6 have been spaced accordingly.

TABLE 7.2

ALLOWED TRANSITIONS FROM $j_i = \frac{3}{2}$ TO $j_f = \frac{1}{2}$ AND THE CORRESPONDING ENERGIES

m_j of final state	m_j of initial state			
	$+\frac{3}{2}$	$+\frac{1}{2}$	$-\frac{1}{2}$	$-\frac{3}{2}$
$+\frac{1}{2}$	$A + \dfrac{3a}{2} - \dfrac{b}{2}$	$A + \dfrac{a}{2} - \dfrac{b}{2}$	$A - \dfrac{a}{2} - \dfrac{b}{2}$	$\times$
$-\frac{1}{2}$	$\times$	$A + \dfrac{a}{2} + \dfrac{b}{2}$	$A - \dfrac{a}{2} + \dfrac{b}{2}$	$A - \dfrac{3a}{2} + \dfrac{b}{2}$

In Table 7.2 are now listed the six transitions from $j = \frac{3}{2}$ to $j = \frac{1}{2}$ in analogy with Table 7–1. However, *since now $a \neq b$*, the spectral line is split into a six-component (symmetric) pattern. This structure of the spectral line is indicated in the lower part of Fig. 7.6; following adopted convention, the components with polarization parallel to the field are indicated above the base line, and with normal polarization below.[†] As before the parallel components have $\Delta m = 0$, the normal ones $\Delta m \pm 1$.

The horizontal spacing between the components is proportional to the differences in the energy of the transition, and the vertical height is pro-

† It is also conventional to label the parallel components with π, and the normal ones by σ (from the German "Senkrecht").

portional to the intensity of the components; the relative intensity can be predicted exactly since it involves only the comparison of matrix elements between the angular parts of the wave function.

As the magnetic field is raised, the separation of the components continues to increase linearly with the field until the separation between Zeeman components becomes of the order of the fine-structure separation (spacing C in Fig. 7.6). At this point the Zeeman components from the $j = \frac{3}{2} \rightarrow \frac{1}{2}$ and $j = \frac{1}{2} \rightarrow \frac{1}{2}$ transition begin to overlap; clearly the perturbation caused by the external magnetic field is of the order of the L·S energy and affects the coupling of L and S into J; J ceases to be a "good quantum number."

For very strong fields, L and S become completely uncoupled, so that the orbital and intrinsic magnetic moments of the electron interact with the field independently, giving rise to an energy shift

$$\Delta E = -\frac{\mu_0}{\hbar} \mathbf{L} \cdot \mathbf{H} - 2 \frac{\mu_0}{\hbar} \mathbf{S} \cdot \mathbf{H} - a \mathbf{L} \cdot \mathbf{S}$$
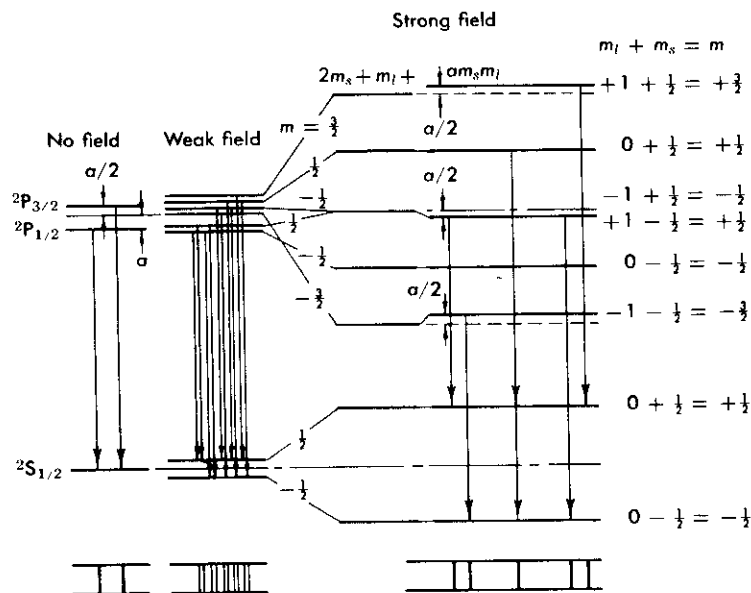
$$= -\mu_0 H (m_l + 2 m_s) - a m_l m_s \qquad (2.15)$$

FIG. 7.7 Energy levels that are the same as Fig. 7.6 but include the region of very strong magnetic field. Note how the sublevels belonging to the $j = \frac{3}{2}$ and $j = \frac{1}{2}$ levels cannot any more be distinguished but have coalesced into five components typical of Fig. 7.2.

Here, m_l and m_s are the projections of L and S on the z axis, and in this case the selection rules for electric dipole transitions become

$$\Delta m_l = 0, \pm 1 \qquad \text{and} \qquad \Delta m_s = 0 \qquad (2.16)$$

In Fig. 7.7 the splitting of the six Zeeman sublevels for the $l = 1, s = \frac{1}{2}$ fine-structure doublet is shown for a weak and for a strong external magnetic field. For weak fields we have the situation already shown in Fig. 7.6 (Eq. 2.14) while in the limit of very strong fields the six sublevels coalesce into five components almost equidistantly split as predicted by Eq. 2.15. However, an additional term must be added to take account of the L·S interaction, which even though weak is still present. As a result, the structure of the spectral line becomes almost a normal Zeeman triplet, as can also be seen in Fig. 7.7. This phenomenon is called the Paschen-Back effect. It necessitates, however, magnetic fields that are beyond the reach of iron core magnets, and thus are difficult to achieve.

2.3 ATOMS WITH MORE THAN ONE VALENCE ELECTRON

In the previous section we discussed the Zeeman effect, including the electron's spin, but only for the case of one (valence) electron outside a closed shell. We have, however, considered in Chapter 2 (Section 4.4) the coupling of the orbital angular momenta $l_1, l_2, \cdots$, of the valence electrons into a resultant L, and of their spins $s_1, s_2, \cdots$, into a resultant S, which then couple to give $\mathbf{J} = \mathbf{L} + \mathbf{S}$. This is the so-called Russell-Saunders coupling and is applicable to mercury; the energy-level diagram and a discussion of the mercury spectrum were given in Chapter 2 (Fig. 2.13).

Let us consider the familiar 5461 Å green line which arises from a transition between the $^3S_1(6s7s)$ state to the $^3P_2(6s6p)$ state. Using Eq. 2.13 we can obtain the g factors for the initial and final state:[†]

$$^3S_1(\ J = 1, L = 0, S = 1) \qquad g_i = 2$$
$$\qquad\qquad\qquad\qquad\qquad\qquad\qquad\qquad (2.16)$$
$$^3P_2(\ J = 2, L = 1, S = 1) \qquad g_f = \tfrac{3}{2}$$

In Fig. 7.8 is given the energy-level diagram for these two states without and with a magnetic field. The structure of the line is indicated in the lower part of the figure and exhibits a symmetric nine-component pattern.

Indeed, the example we are considering involves the same angular momenta $l_i = 1, l_f = 2$ as the example discussed in Section 2.1, where we concluded that only three components would appear because of the equality of the splitting a of the initial level, and of the splitting b, of the final level

[†] Note that we use in Eq. 2.13 L, S, and J, the quantum numbers for the coupled angular momenta of the two valence electrons.
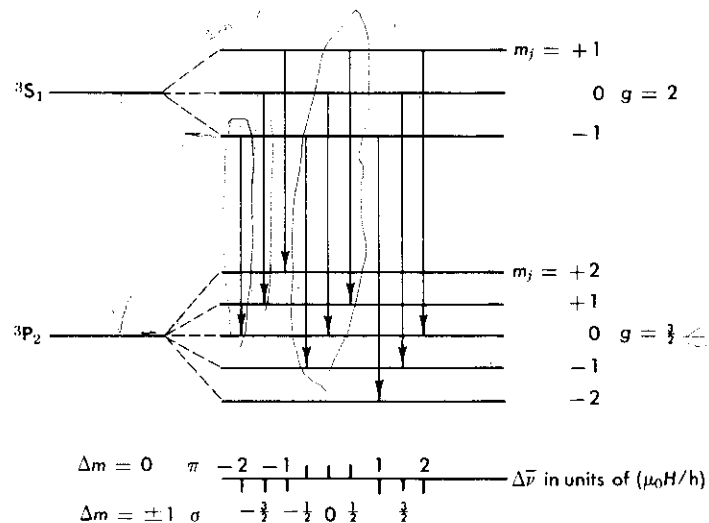
FIG. 7.8   Structure of the Zeeman multiplet arising in a transition from a $^3S_1$ to a $^3P_2$ line; the mercury green line at 5461 Å is an example of such a transition. Note that the situation here is similar to that indicated in Fig. 7.3 if the initial and final state are interchanged.

(Table 7.1). However, in the present instance, the different g factors (Eq. 2.16) make $a \neq b$ and give rise to *all* nine components; the experimental data obtained on the Zeeman effect of this spectral line and discussed in Section 6 below do confirm the structure predicted by Fig. 7.8.

3. Hyperfine Structure

3.1 MAGNETIC DIPOLE INTERACTION

As stated in the introduction, spectral lines, when examined under high resolution, do show a small structure even when no magnetic field is applied. It was also mentioned that such hyperfine structure is due to the interaction of the higher moments of the nucleus with the electromagnetic field of the valence electron or electrons. We will defer the more general treatment of the multipole moments of the nucleus to Section 3.4 and will first discuss only the interaction of the nuclear dipole magnetic moment.

If we consider a nucleus with an intrinsic angular momentum (spin) I different from zero ($I \geq \frac{1}{2}$), we can expect that the revolving charge of the nucleus will give rise to a magnetic moment (see Eq. 2.2) oriented along the spin axis.

$$ \pmb{\mu} = -\frac{e}{2Mc}\mathbf{I} $$

where M is the mass of the nucleus. In addition, nuclei exhibit an intrinsic magnetization†, so that in general we have

$$ \pmb{\mu} = -g_I\frac{e}{2m_pc}\mathbf{I} = g_I\mu_N I\mathbf{u}_I $$

where $\mathbf{u}_I$ is a unit vector along the spin direction, and

$$ \mu_N = \frac{e\hbar}{2m_pc} $$

is the nuclear magneton; m_p is the proton mass. The numerical factor g_I includes all the effects of intrinsic and orbital magnetization of the nucleus and can be obtained only from a theory of nuclear structure.
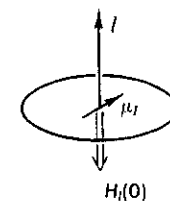

FIG. 7.9   Interaction of the nuclear magnetic moment with the magnetic field produced by the electrons at the nucleus.

Clearly, such a magnetic moment of the nucleus, $\pmb{\mu}$, will interact with the magnetic field $\mathbf{H}_e(0)$ produced by the atomic electrons (at the nucleus; Fig. 7.9). This interaction then results in a shift of the energy levels of the atom (electrons + nucleus, system) by the amount

$$ \Delta E = -\pmb{\mu} \cdot \mathbf{H}_e(0) \tag{3.3} $$

The direction of $\mathbf{H}_e(0)$ is that given by the total angular momentum of the atomic electrons, namely, $\mathbf{J}$,‡ so that

$$ \Delta E = +\left(\frac{\mu}{|I|}\right)\left(\frac{H_e(0)}{|J|}\right)\mathbf{I}\cdot\mathbf{J} \tag{3.4} $$

Thus, we expect the splitting of a level of given J according to the possible values of $(\mathbf{I}\cdot\mathbf{J})$ which as we know are quantized. As a matter of fact, the situation is analogous to that of the fine structure, where the interaction was proportional to the $(\mathbf{L}\cdot\mathbf{S})$ term. In that instance the two angular momenta coupled into a resultant $\mathbf{J} = (\mathbf{L} + \mathbf{S})$ according to the quantum-mechanical laws of addition of angular momentum. In the present situa-

---

† This gives rise to the so-called "anomalous" magnetic moment of the nucleon; for example, the neutron (an uncharged particle) has a magnetic moment of $-1.91\ \mu_N$.

‡ The direction of $\mathbf{H}_e(0)$ is really opposite to $\mathbf{J}$ because the electron has negative charge.
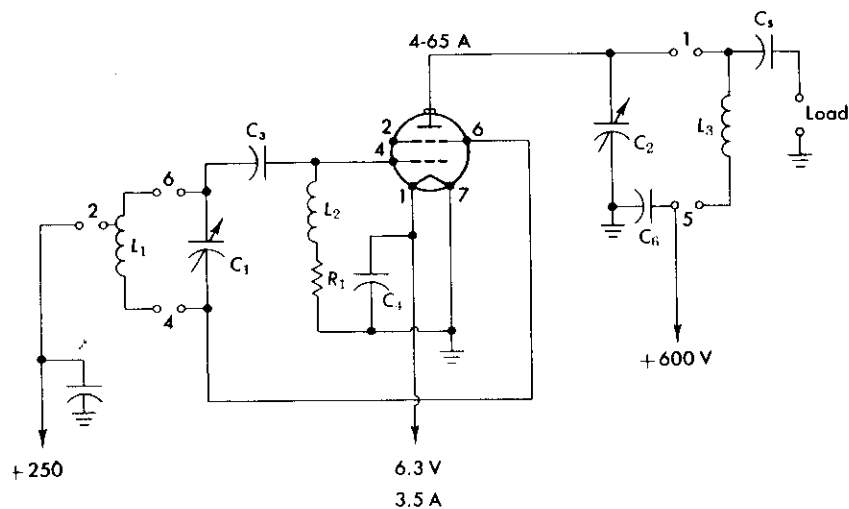
FIG. 7.15   A radio frequency oscillator suitable for exciting an electrodeless discharge
be. Such a source emits spectral lines of narrow width.

L_1 = 20 turns No. 16 wire 1½ dia. 1⅝L tapped 6½	C_3 = 3800$\mu\mu$F
L_2 = 7 turns No. 16 wire ¾ dia. 1⅝L	C_4 = 0.02μF 600 V
L_3 = 7MC BUD-OE L-40	C_5 = 0.01μF 5000V
C_1 = 100$\mu\mu$F	C_6 = 0.1μF 3000V
C_2 = 200$\mu\mu$F	R_1 = 5K 20W

rption cross section; this will be strongest in the center of the line and
eaker in the wings. The result shown in Fig. 7.14a is that the line becomes
squashed" in the center; that is, it is broadened.

If now the outer layers of the source are much cooler than the middle
1es, the width of the particular energy level (due to the Doppler effect)
smaller in the outer layers and absorption takes place only at the central
equency with almost none in the wings. The result is a "self-reversed"
1e as shown in Fig. 7.14b. This effect is very pronounced in the sodium D
nes, and when it is viewed with a high-resolution instrument, the line
:hibits a doublet structure which is frequently mistaken for hyperfine
ructure.

In this laboratory when a commercial high-pressure sodium light is used
ir the alignment of the Fabry-Perot interferometer, each D line gives rise
) a double ring pattern. The separation between centers is of the order of
)pproximately 0.100 cm^{-1} and is a function of the operating voltage, in-
cating that it is due to self reversal.†

In order to avoid these causes of spectral line broadening, special sources
ive been developed. They must radiate lines whose width is as close as

† The hyperfine structure pattern of the sodium D lines is 0.065 cm^{-1} wide.

possible to the natural one, but they must also be quite intense, since high-
resolution instruments by necessity have small luminosity. The sources most
commonly used are the hollow cathode and the electrodeless discharge.

In this laboratory the electrodeless discharge is used. It consists of a
narrow tube (pyrex or quartz) containing a separated mercury isotope
(198) and filled with 10 mm of neon. A radiofrequency or microwave source
is coupled to it by means of clip-leads or a wave guide and provides the
power for sustaining the discharge; the source usually has to be started
with a spark (Tesla) coil. The source may be cooled with an air blast, or
by other means, to dissipate the power absorbed by the glass envelope;
Fig. 7.15 shows the 7 Mc 50-watt radiofrequency oscillator used in this
laboratory to excite the source; the tuning condenser is adjusted for maxi-
mum brilliance or as desired. The Hg^{198} source operated in this fashion
yielded lines of half width at half maximum of the order of $\Delta\bar{\nu} = 0.030$ cm^{-1}.

If a quartz (or vycor) envelope is used for the source (as it must be when
ultraviolet lines are investigated), the experimenter must always wear
glasses. As is well known, even *short exposures* of the eye to ultraviolet light
cause damage, sometimes permanent; strong ultraviolet mercury lines even
cause sunburn of the skin.

5. The Fabry-Perot Interferometer

5.1 GENERAL DISCUSSION

As mentioned in the introduction, the Fabry-Perot is the most commonly
used of the "multiple-beam" interferometers; other instruments in this
category are the Lummer-Gehrcke plate and the Michelson échelon. The
Fabry-Perot has found many uses, such as the measurement of refractive
indices of gases, measurement of lengths, and so on, but here we will be
mainly concerned with its application to the measurement of very small
differences in wavelengths such as appear in the Zeeman effect and hyper-
fine structure.

The Fabry-Perot consists of two parallel flat glass plates, coated on
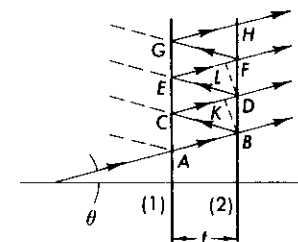the inner surface with a partially transmitting metallic layer. Consider

FIG. 7.16   Reflected and transmitted rays at the
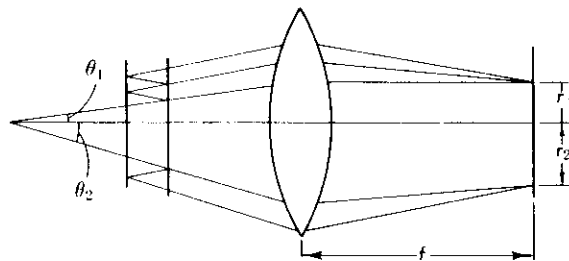two parallel surfaces (1) and (2) of a Fabry-Perot
étalon. The étalon spacing is t.

Fig. 7.17 Focusing of the light emerging from a Fabry-Perot étalon. Light entering the étalon at an angle θ is focused onto a ring of radius $r = f\theta$ where f is the focal length of the lens.

then, the two partially transmitting surfaces (1) and (2) shown in Fig. 7.16 and separated by a distance t. An incoming ray making an angle θ with the normal to the plates will be split into the rays AB, CD, EF, etc. The path difference between the wave fronts of two adjacent rays—for example, AB and CD—is

$$\delta = BC + CK$$

where obviously BK is normal to CD. Then†

$$\delta = 2t \cos \theta$$

and for constructive interference to occur

$$n\lambda = 2t \cos \theta \qquad (5.1)$$

where n is an integer; Eq. 5.1 is the basic interferometer equation. If the refractive index of the medium between the plates is $\mu \neq 1$, we must modify Eq. 5.1 to

$$n\lambda = 2\mu t \cos \theta \qquad (5.1a)$$

Let the parallel rays B, D, F, etc., be brought to a focus by the use of a lens of focal length f as shown in Fig. 7.17. Then when θ fulfills Eq. 5.1a, bright rings will appear in the focal plane, their radius being given by

$$r = f \tan \theta \simeq f\theta \qquad (5.2)$$

Next we wish to find the intensity of the rings (fringes) and the contrast between bright fringes and background. Let the transmission coefficient be T, and the reflection coefficient be R (for no absorption at the surface $R = 1 - T$); and let the intensity of the incident radiation have an am-

---

†
$$CK = BC \cos 2\theta, \quad \text{and} \quad BC \cos \theta = t$$
hence
$$\delta = BCK = BC(1 + \cos 2\theta) = 2BC \cos^2 \theta = 2t \cos \theta$$

plitude A and therefore intensity I_0 where $I_0 = A^2$. The intensities of the rays that are transmitted through the second surface, B, D, etc., are obtained by squaring their amplitudes. Thus

$$I_B = (AT)^2 = I_0 T^2$$

$$I_D = (ARRT)^2 = I_0 R^4 T^2 \text{ etc.}$$

The amplitudes between adjacent rays decrease as R^2, and, therefore, unless R is close to 1, the interference maxima are not sharp. As R is increased, however, T decreases,† and one might suppose that the intensity of the rings would be greatly diminished; this is not true, since now the amplitudes of many rays can be added. The summation over all amplitudes, taking into account the change in phase, is given by Airy's formula:

$$I_T = \left[\sum_{N=1}^{\infty} A_N \right]^2 = I_0 \frac{T^2}{(1-R)^2} \frac{1}{1 + [4R/(1-R)^2] \sin^2 \delta/2} \qquad (5.3)$$

with

$$\delta = 2\pi \frac{2t}{\lambda} \cos \theta$$

We note that at the maxima ($\delta = 0, 2\pi, \cdots$)

$$I_T = \frac{I_0 T^2}{(1-R)^2} \qquad (5.4)$$

which for no absorption yields $I_T = I_0$; at the minima, ($\delta = \pi, 3\pi, \cdots$)

$$I_T = I_0 \frac{T^2}{(1+R)^2} \qquad (5.5)$$

which for no absorption yields $I_T = I_0(1-R)^2/(1+R)^2$ showing that for R close to 1, a very good contrast can be achieved. The intensity distribution of the fringes for different values of R is shown in Fig. 7.18, and clearly high values of R, >0.90 are desirable.

It is important to note the following points:

(a) Since the interfering rays emerging from the interferometer are parallel, they must be focused by a lens of good quality (see Fig. 7.17).

(b) The order of interference n is, in general, very large [$n_0 = (2t)/\lambda$] but the rings that are observed are only from the few orders‡

$$n = (n_0 - \epsilon) - (p - 1) \qquad (5.6)$$

where $p = 1, 2, \cdots$ may be as high as 10.

---

† Typical values for a good interferometer are $R = 0.96$; $T = 0.04$.
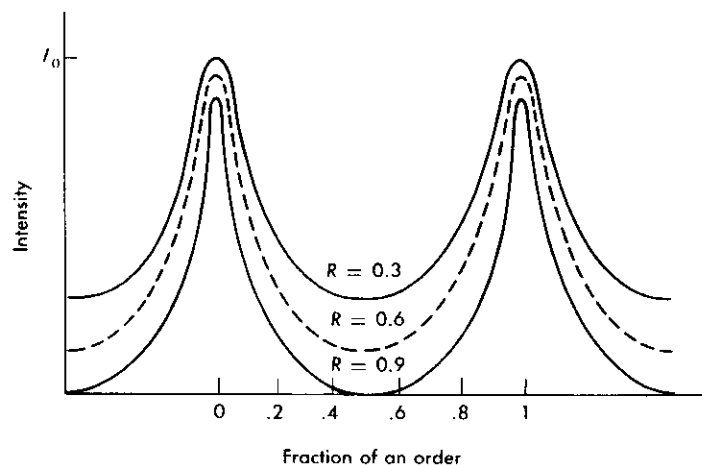‡ Equation 5.6 is discussed in Section 5.3.

FIG. 7.18   The intensity of light from a Fabry-Perot étalon (viewed in the focal plane of the lens) as a function of radial displacement in units of separation between successive orders. R is the reflection coefficient of the interferometer plates; the contrast improves rapidly for increasing R.

(c)   Since interference occurs for rays making an angle θ with the normal to the plates, a *perfectly* parallel beam may not produce fringes. Since we are interested only in small angles θ, an *almost* parallel beam is allowed to be incident on the interferometer; this is achieved by using an extended source at the focus of the first lens (see Fig. 7.21).

5.2 THE FABRY-PEROT ÉTALON

The multiple-beam interferometer discussed above is easily realized in practice. Two *optically flat* glass or quartz plates with one surface coated with an appropriate reflecting film are used. The plates are assembled in a holder (see Fig. 7.19) and held apart by three very accurately machined spacers. Three spring-mounted screws are used to apply pressure, and by
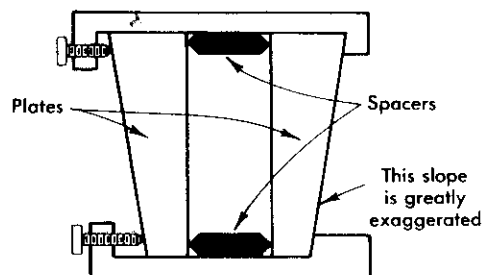

FIG. 7.19   Mounting of the interferometer plates into a Fabry-Perot étalon. Note that the slight slope of the two sides of a plate is usually of the order of 1/10 degree.

careful adjustment, the plates are made parallel. Such an assembly is frequently called a Fabry-Perot étalon.

The plates can be ground flat to $\lambda/20$ (approximately 250 Å), and usually the outer surface is slightly inclined (about 0.1°) with respect to the inner one in order to avoid multiple reflections, which give rise to "ghost" fringes. The reflecting coating is deposited by evaporation in vacuum and is either silver or aluminum depending on the wavelength that will be investigated. Also multilayers of dielectrics are now commonly used. Figure 7.20 gives the reflectivity of these metals as a function of wavelength, but for thick coatings. For thin layers, the reflectivity increases with the thickness of the metal film (but so does the absorption, A); with a film 500 Å thick we may obtain $R = 0.94$, $T = 0.02$, and $A = 0.04$. Note that the performance of the interferometer depends primarily on the quality of these coatings.
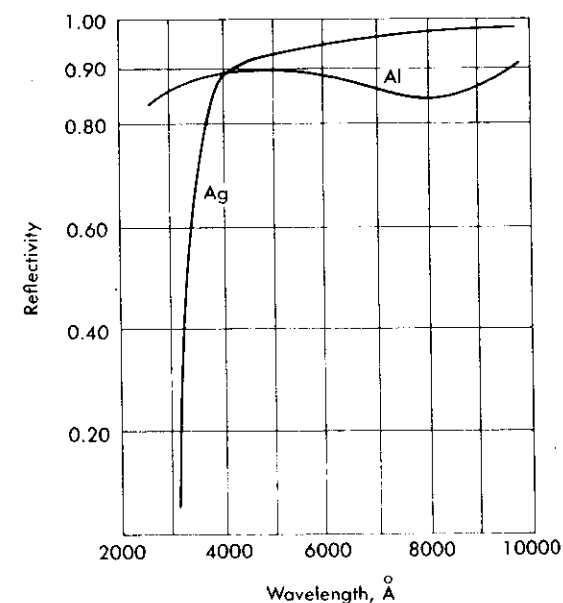

FIG. 7.20   The reflectivity of aluminum and silver coatings as a function of wavelength.

It is also important that the spacers be equal and accurately machined. They can be made of quartz and should also be ground to a $\lambda/20$ precision. It is possible to use several sets of spacers of different length with the same pair of plates; this modifies the spectral range of the étalon, which is given by $\Delta\bar{\nu} = 1/2t$ cm^{-1}.

When long exposures are taken, attention must be given to the stability of the system. The air between the plates must be kept at constant tem-

perature in order that the refractive index† entering Eq. 5.1a does not change; this can be achieved by enclosing the étalon in an insulated box.

It is clear that when a source containing several wavelengths, for example, an atomic spectrum, is viewed with a Fabry–Perot, the ring patterns from all wavelengths are superimposed. To separate the patterns and view only the fringes of the line of interest, a low-dispersion spectrometer is used in conjunction with the Fabry–Perot. The ring pattern is focused onto the slit of the spectrometer, in the focal plane of which now appear vertical sections of each ring pattern, but these are dispersed according to the wavelength. We speak of "crossing" the Fabry–Perot with the spectrometer. Good grating spectrographs are occasionally used for that purpose, but a small prism spectrograph is usually adequate. There are basically two methods for introducing the Fabry–Perot étalon in the optical system: (a) a parallel beam arrangement as shown in Fig. 7.21a, or (b) a converging beam as shown in Fig. 7.21b.
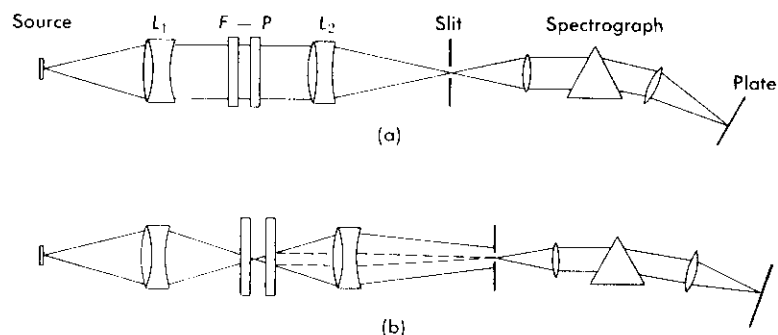

FIG. 7.21 Two possible arrangements for crossing a Fabry-Perot étalon with a low-resolution spectrograph; L_1 and L_2 are compensated lenses and F–P indicates the position of the étalon. (a) The Fabry-Perot is placed in a quasi-parallel beam originating from an extended source. (b) The image of the source is focused onto the Fabry-Perot.

In method (a), lens L_2 focuses the ring pattern onto the spectrometer slit; care must be taken that it be properly adjusted. Maximum light intensity is used with such an arrangement. In method (b), the light source is focused by means of lens L_1 halfway between the Fabry–Perot plates; and the ring pattern is focused by means of L_2 onto the slit. This method has the advantage of easier adjustment of the plates for parallelism and of producing sharper fringes. In both methods the diameter of the rings is

---

† The reader may verify that small changes in temperature may shift the ring pattern by a whole fringe.

determined by the focal length of L_2 and the magnification of the spectrograph, which is frequently 1:1 (the ratio of collimator and camera lens focal lengths).

FIG. 7.22 Two possible arrangements of the spectrograph slit with respect to the Fabry-Perot ring pattern. (a) Off-center method, (b) the center of the pattern as well as two segments of each ring appear on the plate.
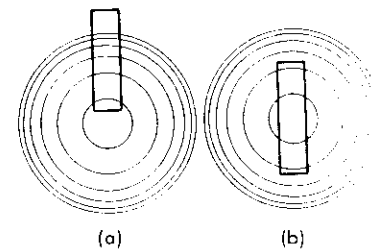
We may project onto the spectrometer slit the central portion of the ring pattern (Fig. 7.22b) or only part of it (Fig. 7.22a). The latter effect can be achieved by tilting the Fabry–Perot étalon (after adjusting the plates) with respect to the optical axis, and leaving the lenses L_1 and L_2 in their original positions. This "off-center" method is used when only a short slit is available, or when the source is so small (not extended) that only few rings can be formed with enough intensity.

5.3 REDUCTION OF THE DATA OBTAINED FROM A FABRY-PEROT

We have seen (Eq. 5.2) that the interference rings formed in the focal plane have radii

$$r_n = f\theta_n \tag{5.2}$$

where the angle θ_n is given by

$$n = \frac{2\mu t}{\lambda}\cos\theta_n = n_0\cos\theta_n = n_0\left(1 - 2\sin^2\frac{\theta_n}{2}\right)$$

and since θ is always small, we obtain

$$n = n_0\left(1 - \frac{\theta_n^2}{2}\right) \quad \text{or} \quad \theta_n = \sqrt{\frac{2(n_0 - n)}{n_0}} \tag{5.7}$$

Now if θ_n is to correspond to a bright fringe, n must be an integer; however, n_0, which gives the interference at the center ($\cos\theta = 1$ or $\theta = 0$ in Eq. 5.1), is in general *not* an integer:

$$n_0 = \frac{2\mu t}{\lambda} \tag{5.8}$$

(There is no bright spot in the center of the pattern, in general.) If n_1 is the interference order of the first ring, clearly $n_1 < n_0$ since $n_1 = n_0\cos\theta_1$. We then let $n_1 = n_0 - \epsilon$, with $0 < \epsilon < 1$ where n_1 is the closest integer to

n_0 (smaller than n_0). Thus, we have in general for the pth ring of the pattern, as measured from the center out,

$$n_p = (n_0 - \epsilon) - (p - 1) \tag{5.6}$$

Combining Eq. 5.6 with Eqs. 5.7 and 5.2, we obtain for the radii of the rings

$$r_p = \sqrt{\frac{2f^2}{n_0}} \sqrt{(p-1) + \epsilon} \tag{5.9}$$

We note (a) that the difference between the squares of the radii of adjacent rings is a constant

$$r_{p+1}^2 - r_p^2 = \frac{2f^2}{n_0} \tag{5.10}$$

and (b) that the fraction of an order ϵ can be found by extrapolating to $r_p^2 = 0$ (according to the slope $2f^2/n_0$).†

Now,‡ if there are two components of a spectral line with wavelengths λ_1 and λ_2, very close to one another, they will have fractional orders at the center ϵ_1 and ϵ_2:

$$\epsilon_1 = \frac{2t}{\lambda_1} - n_1(1) = 2t\bar{\nu}_1 - n_1(1)$$

$$\epsilon_2 = \frac{2t}{\lambda_2} - n_1(2) = 2t\bar{\nu}_2 - n_1(2)$$

where $n_1(1)$, $n_1(2)$ is the order of the first ring. Hence, if the rings do not overlap by a whole order ($n_1(1) = n_1(2)$), the difference in wave numbers between the two components is simply

$$\bar{\nu}_1 - \bar{\nu}_2 = \frac{\epsilon_1 - \epsilon_2}{2t} \tag{5.11}$$

If the orders are overlapped x times,

$$\bar{\nu}_1 - \bar{\nu}_2 = \frac{x + \epsilon_1 - \epsilon_2}{2t} \tag{5.11b}$$

From Eq. 5.11 we see that we do not need to know t much more accurately than $\epsilon_1 - \epsilon_2$. The fractional order ϵ_1, ϵ_2, $\cdots$, can hardly be measured to 1/1000; therefore knowledge of t to this accuracy of 1/1000 is amply adequate; this can be easily achieved with a micrometer or a microscope.

† See also Fig. 7.28.
‡ From here on we set $\mu = 1$.

The resolution† of the Fabry–Perot can be obtained from Eq. 5.1:

$$\bar{\nu} = \frac{1}{\lambda} = \frac{n}{2t \cos \theta}$$

and by differentiation

$$\Delta\bar{\nu} = \frac{\Delta n}{2t} \left[\frac{1}{\cos \theta} - \frac{n \sin \theta}{\cos^2 \theta} \right] \tag{5.12}$$

and since θ is always small

$$\Delta\bar{\nu} \simeq \frac{1}{2t} \Delta n \tag{5.13}$$

where Δn is the *fraction of order* by which one ring pattern is shifted with respect to an other. (Note that when this fraction of order is measured at the center, Eq. 5.13 becomes exact, and since $\Delta n(\theta = 0) \equiv \epsilon_1 - \epsilon_2$ we get back Eq. 5.11.)

The fraction of order Δn that can be measured experimentally depends on the quality of the plates (as shown by Eq. 5.5, contrast of fringes), on the proper alignment and *focusing* of the optical system, and on the width and relative intensity of the components that are being measured. Values of $\Delta n \approx 1/100$ are common, and with some care this value can be exceeded‡.

Using $\Delta n = 1/100$, we then find for the resolving power of the Fabry–Perot at a wavelength of $\lambda = 5000$ Å and a spacing $t = 0.5$ cm

$$\frac{\Delta\bar{\nu}}{\bar{\nu}} = \Delta n \left(\frac{\lambda}{2t}\right) = 10^{-2} \times 5 \times 10^{-5} = 5 \times 10^{-7} \tag{5.14}$$

which is quite satisfactory. In general, we see that the wave number interval between adjacent rings (called the free spectral range) is

$$\Delta\bar{\nu} \text{ (for } \Delta n = 1) \simeq \frac{1}{2t}$$

which can be used as a "scale factor" for the frequency difference of any components appearing in the spectral line.

In reducing the data our aim is to obtain the orders of fractional interference ϵ_1, ϵ_2, $\cdots$, for all the components of the line, and also to know if any of the components overlap in order, and in that case by how many orders.

† See also Eq. 1.5a.
‡ For example, for the data discussed in Section 6.2, and presented in Fig. 7.27, Δn is of the order of approximately 1/20.

The possibility of components overlapping in order increases when a large spacing is used ($\Delta\bar{\nu}$ between adjacent fringes is small). To clear up such ambiguity, exposures of the same line are obtained with two or three different sets of spacers, providing also consistency checks of the assignments that were made.

As stated before, we may obtain a Fabry-Perot pattern containing the center of the ring system as shown in Fig. 7.22b. In that case we work with rings close to the center so as to extract the fractional order ϵ for each component. Alternatively, we may obtain a pattern not containing the center as shown in Fig. 7.22a, in which case we use only the pth to the $(p + q)$th rings; this is known as the off-center method.

We will be concerned with the first method, and let R_p be the radius of the pth ring as measured on the photographic plate. Note that it is possible to measure R_p only if the center of the pattern is included on the plate. The fractional order ϵ is then given by Eq. 5.15 below, which follows from Eq. 5.9

$$\frac{R_{p+1}^2}{R_{p+1}^2 - R_p^2} - p = \epsilon \tag{5.15}$$

We note that the denominator in Eq. 5.15 is a constant, and any adjacent pair of rings can yield a value for ϵ. However, since the squares of the radii of successive rings are linearly related (they form an arithmetic progression) in order to utilize all available information a least squares fit to Eq. 5.15 must be made.

A somewhat less tedious reduction technique, in which the squares of the radii and their differences are tabulated in a square array, is given by Tolansky.† Consider a line which has three components a, b, c, and let the respective radii be $R_{1a}, R_{2a}, R_{3a}, \cdots$, for component a; $R_{1b}, R_{2b}, R_{3b}, \cdots$, for component b, and similarly for c. From Eq. 5.10 it is clear that the difference between the squares of the radii of component a,

$$\Delta_a = R_{(p+1),a}^2 - R_{p,a}^2 = \frac{2f^2}{n_{0,a}}$$

is equal (to within a very small part) to the same difference for component b,

$$\Delta_b = R_{(p+1),b}^2 - R_{p,b}^2 = \frac{2f^2}{n_{0,b}}$$

or any other component of the same line; let these differences be designated

† S. Tolansky, *High Resolution Spectroscopy*, Methuen, London, 1947, p. 130.

by Δ. Now from Eq. 5.15,

$$\epsilon_a = \frac{R_{(p+1),a}^2}{\Delta} - p$$

$$\epsilon_b = \frac{R_{(p+1),b}^2}{\Delta} - p \text{ etc.}$$

and the required separation (in wave numbers) between the two components, a and b, is

$$\Delta\bar{\nu} = \frac{\epsilon_a - \epsilon_b}{2t} = \frac{R_{p,a}^2 - R_{p,b}^2}{\Delta} \times \frac{1}{2t} \tag{5.16}$$

If we designate by $\delta_{a,b}^p$ the difference between the square of the radii of the pth order rings of components a and b, and by $\Delta_{p,p+1}^2$ the difference between the square of the radii of the pth and $(p + 1)$th ring of component a, we can form the square array shown in Table 7.4. We note that all Δ's

TABLE 7.4
SQUARE ARRAY FOR REDUCTION OF FABRY-PEROT DATA

Component	Ring number									
	1		2		3		4		5	
a	R_{1a}^2	Δ_{12}^a	R_{2a}^2	Δ_{23}^a	R_{3a}^2	Δ_{34}^a	R_{4a}^2	Δ_{45}^a	R_{5a}^2	etc ...
	δ_{ab}^1		δ_{ab}^2		δ_{ab}^3		δ_{ab}^4		δ_{ab}^5	
b	R_{1b}^2	Δ_{12}^b	R_{2b}^2	Δ_{23}^b	R_{3b}^2	Δ_{34}^b	R_{4b}^2	Δ_{45}^b	R_{5b}^2	etc ...
	δ_{bc}^1		δ_{bc}^2		δ_{bc}^3		δ_{bc}^4		δ_{bc}^5	
c	R_{1c}^2	Δ_{12}^c	R_{2c}^2	Δ_{23}^c	R_{3c}^2	Δ_{34}^c	R_{4c}^2	Δ_{45}^c	R_{5c}^2	etc ...

must have the same value in any one row, and *also* in any column. Thus when an error in measurement has been made, it becomes immediately apparent, and that radius can be rejected. Similarly all δ's in one row must be equal and their average can be taken. To obtain $\Delta\bar{\nu}$, we first obtain the average value of Δ; however, we should not use every available Δ, but only alternate† ones to obtain the average. Then the average value of the

† Note that if we take

$$\langle\Delta\rangle = (1/k)(\Delta_{12} + \Delta_{23} + \cdots + \Delta_{k,k+1})$$

this is equivalent to

$$(1/k)[(R_2^2 - R_1^2) + (R_3^2 - R_2^2) + \cdots + (R_{k+1}^2 - R_k^2)] = (1/k)(R_{k+1}^2 - R_1^2)$$

so that only the information from the first and last ring is used.

δ's is obtained and

$$\Delta \bar{\nu}_{ab} = \frac{\langle \delta_{ab} \rangle}{2t \langle \Delta \rangle} \qquad (5.16a)$$

This method of reduction of the data is quite satisfactory, and use of it will be made in the next section.

For an "off-center" pattern this technique is not applicable, since the radii are not known. The data reduction is based on the fact that now the difference in radii (not in the square of radii) of adjacent rings is almost a constant.†

6. The Zeeman Effect of the λ = 5461 Å Line of Hg^198

6.1 EQUIPMENT AND ALIGNMENT

We now consider the observation in this laboratory of the Zeeman effect on the λ = 5461 Å line of Hg^198. The choice of the green line is due to its predominance in the mercury spectrum, and the ease with which it can be observed. In an external magnetic field, it is split into nine components, as discussed in detail in Section 2.3. In the present observations, a polarizer parallel to the magnetic field was used, so that only three of the nine components (the π light) appeared. Furthermore, natural mercury exhibits in the green line a large number of hyperfine structure components, and each of them forms a Zeeman pattern. To avoid a multiplicity of components in one spectral line, a separated isotope of mercury was used as the source. Hg^198 is well suited for our purpose since $I = 0$, and therefore
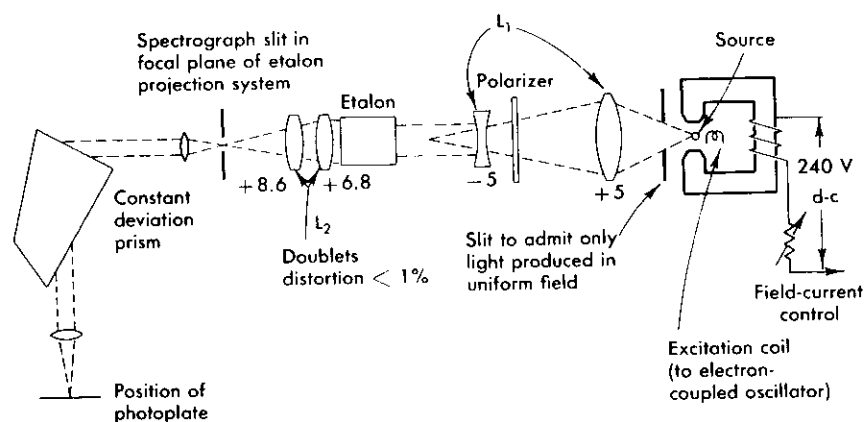

FIG. 7.23 Experimental arrangement used for observing the Zeeman effect with a Fabry-Perot étalon, crossed by a constant deviation prism spectrograph.
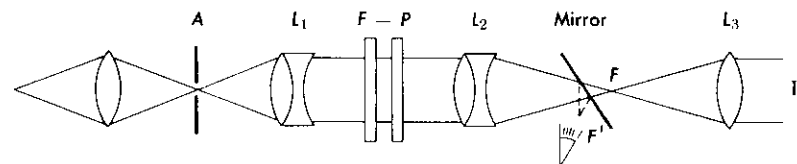
† See also Tolansky, loc. cit.

FIG. 7.24 Optical arrangement for aligning a Fabry-Perot étalon. Rough adjustment is made by viewing the image formed by L_3. Final adjustment is made by viewing the plates from the point F (or F'). Patterns as shown in Fig. 7.25 will be observed.

it exhibits no hyperfine structure; Hg^198 is usually obtained by neutron capture in gold

$$_{79}Au^{197} + n \rightarrow {}_{80}Hg^{198} + e^-$$
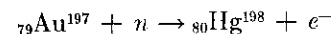
and subsequent separation by chemical methods of the mercury from the gold.†

The optical system used for this investigation is shown in Fig. 7.23. The Fabry-Perot was crossed in the parallel-beam method with the small constant-deviation spectrograph described in Chapter 2. The étalon and lenses are all mounted on an optical bench to which the spectrograph is rigidly attached. The pair of lenses L_1 forms the light from the source into a parallel beam, while the pair L_2 focuses the Fabry-Perot ring pattern onto the spectrograph slit; the effective focal length of L_2 is 8 cm, and a further magnification of 2 takes place in the spectrograph.

The discharge tube is mounted vertically, as is the spectrograph slit; the slit width was 1 mm. It is clear that in this arrangement not only the ring pattern is focused onto the spectrometer slit but also the image of the source. A sheet of polaroid that could be rotated at will was used as a polarizer.

The spacing of the Fabry-Perot étalon is

$$t = 0.5002 \text{ cm}$$

and it is imperative to adjust the plates carefully for parallelism. This can be done either by viewing through the spectrograph with a frosted glass in the focal plane, and adjusting for the best quality of the pattern, or by a much more sensitive arrangement as shown in Fig. 7.24. A very small aperture (less than 1 mm in diameter) is placed at the position of the source and illuminated with an intense sodium lamp. The Fabry-Perot plates are adjusted to be normal to the optical axis by bringing the image of A reflected by the étalon back onto A. Next, L_3 is adjusted until a series of multiple images of A appears when the observer is located at I; the plates of the étalon can then be roughly adjusted for parallelism by bringing all

† Ready-made Hg^198 electrodeless discharge tubes can be obtained from the Ryan, Velluto, and Anderson Glass Works, Inc., in Cambridge, Mass., or from other suppliers.
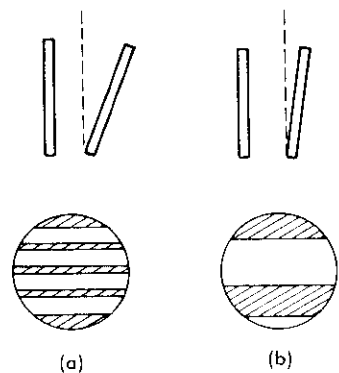
FIG. 7.25   Patterns seen on the axis in the focal plane of a Fabry-Perot when illuminated with a point source. (a) Poor plate parallelism, (b) improved plate parallelism. The tilt of the plates shown is greatly exaggerated.

the images into coincidence. The final adjustment is made by removing L_3 so that the observer locates his eye at F (or a mirror can be used); then, fringes of equal width do appear parallel to the base of the wedge that is formed by the two plates (Fig. 7.25). As the plates are moved into parallelism, the fringes become broader and finally the whole image of the aperture A seems to have a uniform illumination (bright or dark depending on the exact value of $n_0 = 2t/\lambda$). It is equally important that the ring pattern be in sharp focus at the plane of the photographic plate. For this experiment Kodak Royal-Pan film was used.

The electrodeless discharge was excited as described in Section 4, and to observe the Zeeman effect the discharge tube was placed in a magnetic field. A small iron core electromagnet powered by a 220-V d-c line was used to produce the field; it was controlled by a bank of resistors and a rheostat.
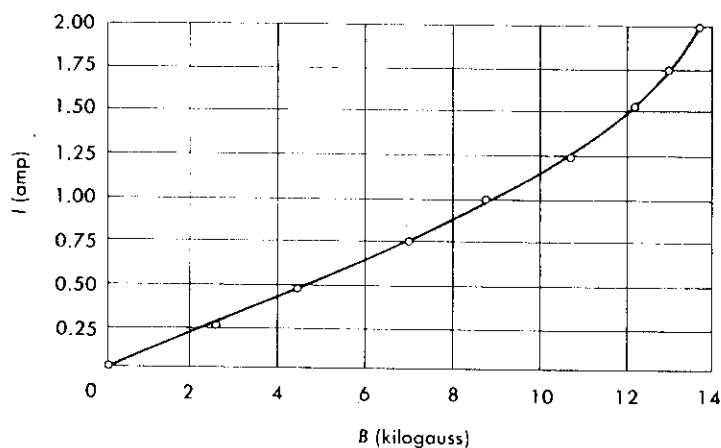

FIG. 7.26   Calibration of the electromagnet used in the Zeeman effect experiment. The magnetic field is plotted against current; note the saturation at high fields.

The diameter of the pole faces was only $1\frac{1}{2}$ in., and a small gap ($\frac{1}{2}$ in.) was used. By tapering the pole faces, higher magnetic fields can be achieved but this reduces the effective area of the field as well as the homogeneity. The magnetic field was measured with a "flip coil" and the calibration of field against current is given in Fig. 7.26. It is seen that field strengths of 12 kilogauss could be reached.

6.2 DATA ON THE ZEEMAN EFFECT

The data presented below were obtained by students[†]. Figure 7.27 shows the Hg 5461 Å line photographed at various magnet settings. As explained earlier, the source contains a single isotope, and the polarizer allows only the observation of π light. We note that the fringes are rather broad, but it can clearly be seen that when the field is applied the single-line pattern (Fig. 7.27a) breaks up into a triplet, the separation between the components of the triplet becoming larger with increasing field.
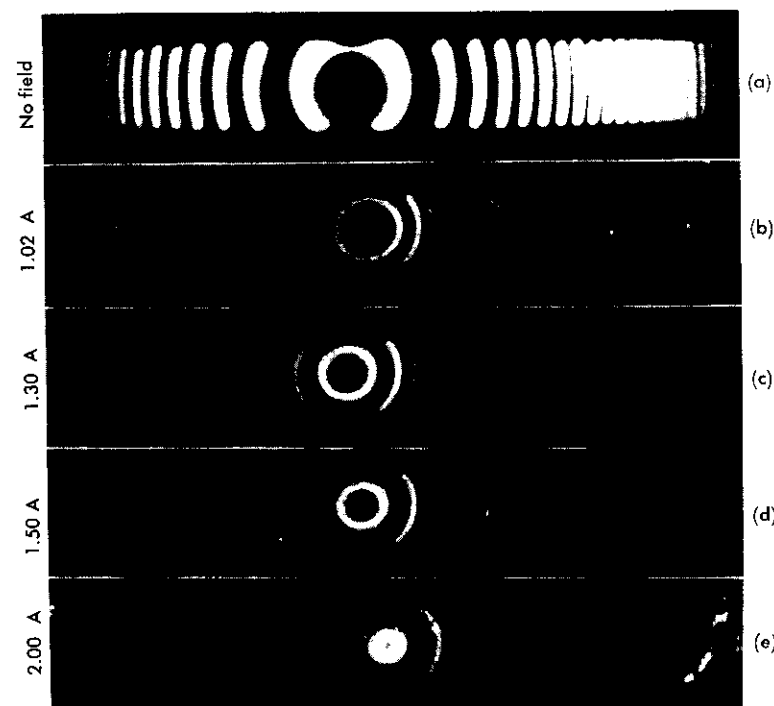

FIG. 7.27   Fabry-Perot patterns showing the Zeeman effect of the green line of mercury. (See the text for additional details.) (a) No magnetic field applied. (b)—(e) A magnetic field of progressively greater strength is applied. Note the splitting of the original line into a triplet of increasing separation.

[†] E. Glover and T. Wagner, class of 1961.

We will first analyze the exposure with zero field in order to verify that the squares of the radii do indeed follow Eqs. 5.9 and 5.10, and we will find the fractional order at the origin by making a least-squares fit to the squares of the radii. Next we will analyze the 1.00-amp and 1.50-amp exposures by the square-array method.

The initial step in the reduction of the data is the measurement of the diameters (or radii) of the rings. To this effect a traveling microscope was used, and readings were taken directly off the plate; care must be taken to insure that the travel of the microscope is indeed along the diameter of the rings and that the crosshairs are properly oriented. When the fringes in the pattern are as broad as in Fig. 7.27, it is much more accurate to measure the two edges and take the average rather than try to set the crosshairs in the center of the fringe. A more advanced technique for obtaining the ring diameters from the plates is to use a microphotometer.

In Table 7.5 are tabulated the radii of the rings, their squares, and the differences of the squares for the exposure with no field. The same data are also plotted in Fig. 7.28, and it is seen that the straight-line fit is quite satisfactory. The fractional order at the center is found to be $\epsilon_0 = 0.595 \pm 0.024$. For the exposures at 1.00 amp (8.7 kilogauss) and 1.50 amp (12.1 kilogauss), the square array, as described in the Section 5.2, is presented in Tables 7.6 and 7.7; it yields the separation in wave numbers of component a from the central component b, and of c from b. Furthermore, if the fractional order of the central component b is calculated as before, it is found to be $\epsilon_1 = 0.649 \pm 0.024$ and $\epsilon_2 = 0.667 \pm 0.014$, respectively, in
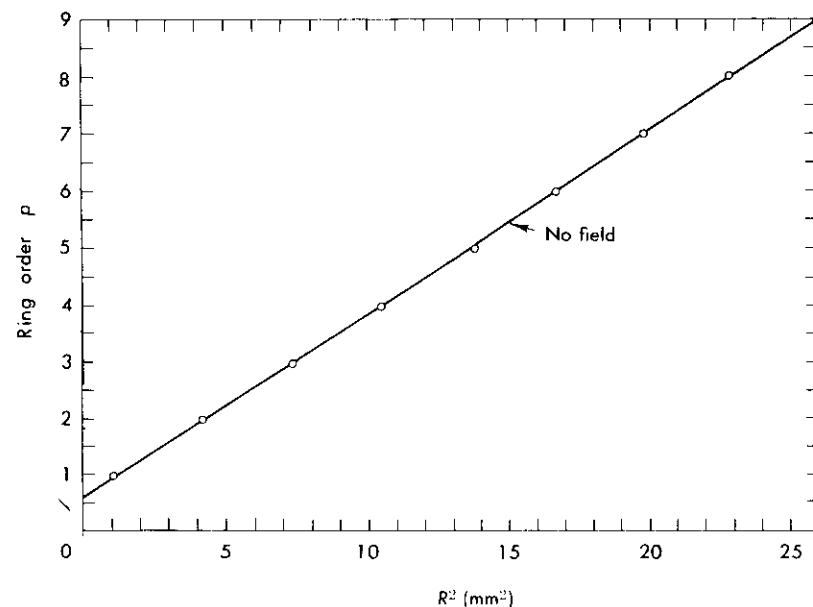

FIG. 7.28   Plot of the square of the Fabry-Perot ring radii against the order of the ring (as measured from the center out). This plot pertains to the data of Fig. 7.27(a) tabulated in Table 7.5 where no magnetic field is applied. The straight line is the least squares fit to the experimental points.

TABLE 7.5
RADII OF FABRY–PEROT PATTERN FOR SINGLE LINE

Ring p	Radius R_p (cm)	R_p^2 (mm^2)	$(R_{p+1}^2 - R_p^2)$ (mm^2)	Ring p	Radius R_p (cm)	R_p^2 (mm^2)	$(R_{p+1}^2 - R_p^2)$ (mm^2)
							3.095
1	0.103	1.071		7	0.444	19.758	
			3.140				2.995
2	0.205	4.211		8	0.477	22.753	
			3.144				3.104
3	0.271	7.355		9	0.508	25.857	
			3.091				3.087
4	0.323	10.446		10	0.538	28.944	
			3.281				2.922
5	0.370	13.727		11	0.564	31.866	
			2.936				2.826
6	0.408	16.663		12	0.589	34.692	

TABLE 7.6
FABRY–PEROT DATA SQUARE ARRAY (FIELD OF 8.7 KILOGAUSS)

Component	Ring order p								
	1	Δ	2	Δ	3	Δ	4	Δ	5
a	0.436	3.136	3.572	3.188	6.760	3.226	9.986	3.118	13.104
δ_{ab}	0.625		0.796		0.692		0.838		0.660
b	1.061	3.307	4.368	3.084	7.452	3.372	10.824	2.940	13.764
δ_{bc}	0.762		0.650		0.784		0.668		0.524
c	1.823	3.195	5.018	3.218	8.236	3.256	11.492	2.796	14.288

Note: All numbers are in mm^2; to evaluate $\langle\Delta\rangle$ we used the six numbers between rings 1–2 and 3–4; to evaluate $\langle\delta\rangle$ we used the information from rings 1–4 only. We obtain

$$\langle\Delta\rangle = 3.249, \qquad \langle\delta_{ab}\rangle = 0.737, \qquad \langle\delta_{bc}\rangle = 0.716$$

and using $t = 0.5002$

$$\Delta\bar{\nu}(a - b) = 0.227 \text{ cm}^{-1}; \qquad \Delta\bar{\nu}(b - c) = 0.220 \text{ cm}^{-1}.$$

TABLE 7.7
FABRY–PEROT DATA SQUARE ARRAY (FIELD OF 12.1 KILOGAUSS)

Component	Ring order p								
	1	Δ	2	Δ	3	Δ	4	Δ	5
a	0.207	3.142	3.349	3.411	6.670	3.289	10.049	2.983	13.032
δ_{ab}	0.917		0.895		0.858		0.841		1.031
b	1.124	3.120	4.244	3.374	7.618	3.272	10.890	3.173	14.063
δ_{bc}	0.921		0.864		0.908		0.806		0.837
c	2.045	3.063	5.108	3.418	8.526	3.170	11.696	3.203	14.900

Note: All numbers are in mm²; to evaluate $\langle \Delta \rangle$ we used the six numbers between rings 1–2 and 3–4; to evaluate $\langle \delta \rangle$ we used all values except the $\delta_{ab} = 1.031$. We obtain

$$\langle \Delta \rangle = 3.176, \qquad \langle \delta_{ab} \rangle = 0.878, \qquad \langle \delta_{bc} \rangle = 0.867$$

and using $t = 0.5002$

$$\Delta\bar{\nu}(a - b) = 0.276 \text{ cm}^{-1}, \qquad \Delta\bar{\nu}(b - c) = 0.273 \text{ cm}^{-1}$$

agreement with the no-field value ϵ_0. Thus we conclude that the central component is not shifted by the application of the magnetic field.

The final data are summarized in Fig. 7.29 where the spacing of the components against magnetic field is shown. We see that the spacing varies linearly with the field, and the proportionality coefficient has the value

$$\frac{\Delta\bar{\nu}}{H} = 0.024 \text{ cm}^{-1}/\text{kilogauss} \tag{6.1}$$

From the discussion of Section 2.3, we know that the Hg 5461 Å line connects the $^3S_1$ and $^3P_2$ states; the structure of the line is indicated in Fig. 7.8. Since the polarizer was set to select only components arising in transitions with $\Delta m = 0$, we expect to observe only the three central components, which will be separated by (Eq. 2.16):

$$\Delta\bar{\nu} = \frac{\mu_0}{hc}(g_i - g_f)H = \frac{1}{2}\frac{\mu_0}{hc}H \tag{6.2}$$

By comparing Eq. 6.2 with the experimental result of Eq. 6.1, we obtain

$$\frac{\mu_0}{hc} = (4.80 \pm 0.5) \times 10^{-5} \quad \text{cm}^{-1}/\text{gauss}$$

in good agreement with the accepted value

$$\frac{\mu_0}{hc} = 4.669 \times 10^{-5} \quad \text{cm}^{-1}/\text{gauss}$$

From these data we conclude that indeed spectral lines are split into
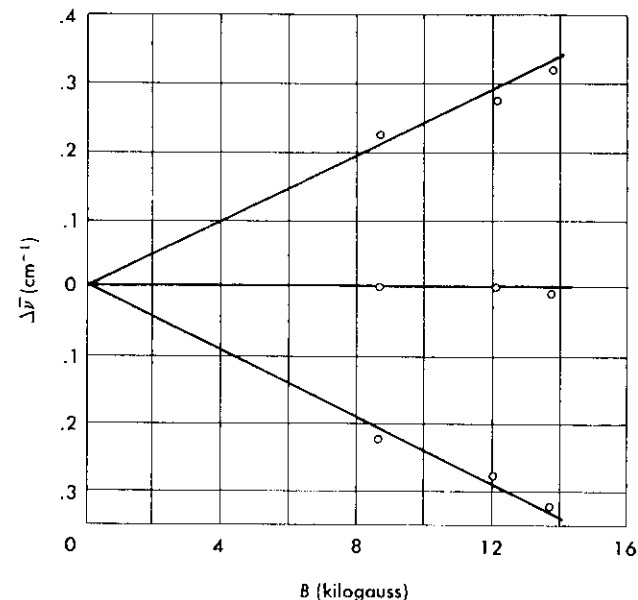
FIG. 7.29   Results obtained on the Zeeman effect of the green line of mercury (see text). The observed displacement of the three components from the zero field value (of the single line) is plotted against magnetic field.

components when the source is placed in a magnetic field. Further, the splitting observed was in excellent agreement with the theory of the anomalous Zeeman effect; the normal Zeeman effect can be excluded, since the energy difference between the components of the line was not $\mu_0 H$ (but instead $\frac{1}{2}\mu_0 H$).

Finally to illustrate the use of the Fabry–Perot in the off-center method, Fig. 7.30 has been included. This exposure was obtained with a high-quality interferometer by Dr. L. C. Bradley III, on the 4047 Å line of Hg¹⁹⁷; the orders shown are from $p = 5$ to $p = 8$. No magnetic field is applied but the hyperfine structure is clearly resolved.

FIG. 7.30   Fabry-Perot pattern of good quality, obtained in the off-center method on the 4047 Å line of Hg¹⁹⁷ (radioactive). The three distinct components observed are due to the hyperfine structure of this line.